Mitigating the Effects of Irregular Reflection Beam Patterns Through Data Association in RIS-Aided mmWave Positioning

Mitigating the Effects of Irregular Reflection Beam Patterns through Data Association in RIS-aided mmWave Positioning

H. Kim*, B. Denis†, M. Rahal‡, T. Mazloum†, R. D'Errico†, and H. Wymeersch§
*Department of Electronics Engineering, Chungnam National University, KOR-34134 Daejeon, South Korea
†CEA-Leti, Université Grenoble Alpes, F-38000 Grenoble, France
‡Institute for Communication Systems, University of Surrey, UK-GU27XH Guildford, The United Kingdom
§Department of Electrical Engineering, Chalmers University of Technology, S-41296 Gothenburg, Sweden

***Abstract*—Despite promising potential for boosting or even simply enabling the localization capabilities of future wireless communication networks, low-complexity reflective Reconfigurable Intelligent Surfaces (RISs) have recently been shown to suffer from practical limitations, such as irregular beam patterns and grating lobes caused by element-wise phase quantization or hardware impairments. The latter phenomena can introduce geometric ambiguities in the RIS-aided positioning problem, when estimating the RIS Angle of Departure (AoD) through beam sweeping based on downlink received power. In this context, our paper introduces an algorithmic framework that combines user position estimation and data association between radio observations and underlying channel model parameters, while still requiring the same basic RIS hardware and UE channel estimation capabilities. Validations based on field measurements centered around 28GHz are provided in a reference indoor environment for different bandwidths, showing the relevance of the proposed solution in terms of both position accuracy and geometric disambiguation.**

***Index Terms*—Data Association, Geometric Ambiguities, Indoor Positioning, Proof-of-Concept Validations, Reconfigurable Intelligent Surface, Side Lobes, Wireless Localization.**

I. Introduction

Reconfigurable Intelligent Surfaces (RISs), which consist of nearly-passive, controllable devices that function as electromagnetic mirrors or lenses, are anticipated to be a pivotal technology for beyond fifth-generation (B5G) wireless systems [1]. These surfaces can indeed enhance the performance of wireless communication networks by manipulating the radio propagation conditions on purpose. In particular, they can contribute to increase throughputs, expand radio coverage or fill dead zones, limit information leakage and unintentional exposure to electromagnetic waves, among other benefits [2]. In the specific localization context, these RISs have theoretically demonstrated their ability to both locally boost accuracy on demand and, even more importantly, make localization feasible in challenging operational scenarios and/or under constrained deployment conditions [3], [4]. For example, the use of reflective RISs has been largely explored for parametric multipath-aided positioning in Line-of-Sight (LoS) [5]–[9] and non-line-of-sight (NLoS) [10]–[12] environments, assuming both far-field or geometric near-field propagation regimes. For performance assessment, most of these contributions still rely on synthetic simulations using oversimplified signal models or at best, lookup tables characterizing the addressable element-wise complex reflection coefficients of RIS prototypes [13].

Single-BS 2D positioning through reflective RIS beam sweeping and received power measurements at the User Equipment (UE) was first experimentally illustrated at 60 GHz in [3], where two RISs were emulated by coupling the receiving and transmitting blocks of distinct transceivers. Another RIS-assisted downlink positioning proof-of-concept was more recently reported in [14], relying on frequency-domain mmWave channel measurements at 26-28GHz [15] with a real RIS hardware prototype [16]. Beyond the shown performance gains, concrete limitations were also pointed out, regarding the presence of grating lobes at the RIS due to 1-bit phase element quantization and hardware impairments, but also the effect of loose uniform discretization of the angular space during RIS beam sweeping and too large RIS-UE distances. The conjunction of these factors lead to the observation of significant undesired power peaks on the receiver side, which can be misinterpreted as resulting from the main lobe of the RIS beam pattern (See Fig. 1). In practice, this phenomenon imposes to select RIS Angle of Departure (AoD) candidates, hence creating geometric ambiguities for positioning.

In this paper, we thus propose an algorithmic scheme combining data association and positioning steps so as to solve the power-based AoD ambiguities induced by such irregular RIS beam patterns, while still coping with the same low-complexity RIS hardware and basic embedded processing capabilities at the UE. More precisely, the proposed approach relies on the computation of the probability density of the user position from the Bayesian perspective. The prior density is determined by the resolvable multipath component exhibiting the shortest time delay, while the posterior density is computed with channel parameters corresponding to other multipath components, thanks to a data association scheme. For performance evaluations, we leverage the same mmWave channel measurements as that initially used in [14]. On this occasion, we also investigate the effect of frequency bandwidth onto the estimation performances.

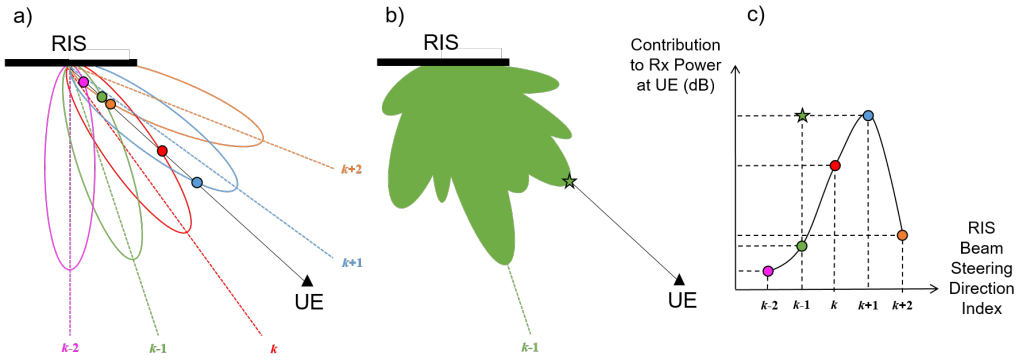

Fig. 1: Combined effects of azimuth discretization and RIS side lobes on power-based AoD estimation: (a) Idealized RIS beam scanning procedure assuming regular beam patterns with a well-formed and dominating main lobe, showing just the impact of the azimuth space discretization when the UE lies in between two steering directions (hence, with limited collected Rx power in comparison with the maximum possible power gain offered at the RIS); (b) Example of a more realistic RIS beam pattern for an arbitrary steering direction $k-1$, with significant side lobes (possibly well aligned with the UE direction) ; (c) Resulting received power collected at the UE as a function of the RIS beam steering direction, for ideal vs. realistic beam patterns (circles vs. triangle), showing an AoD ambiguity (btw. directions $k-1$ and $k+1$).

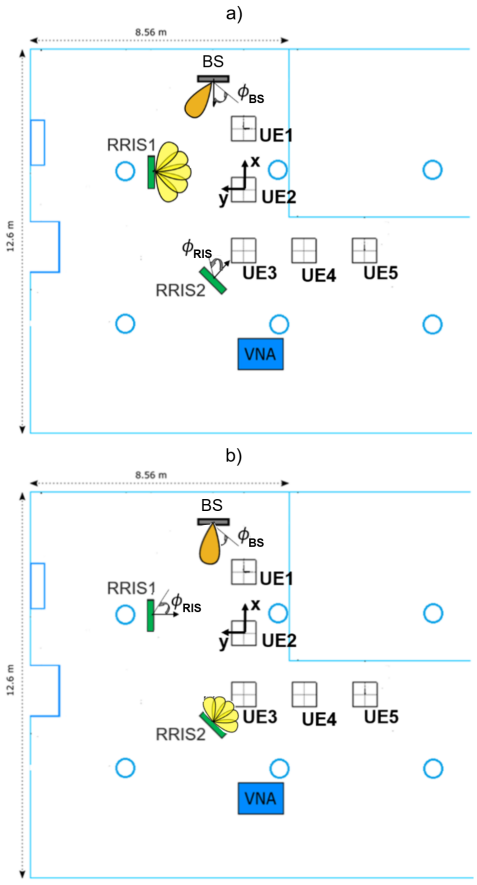

Fig. 2: Layout and deployment considered in the mmWave channel measurement campaign used for validation [15], including 1 BS location, 2 RIS locations (RRIS1 in a) and RRIS2 in b)) and 5 UE locations (UE1 to UE5).

II. mmWave Measurements

A. Experimental Setup and Measurement Procedure

The experimental setup relies on a Vector Network Analyzer (VNA)-based mmWave channel sounder [15]. It includes a transmit-array [17] on the Transmitter (TX) side and a reflective RIS [16] between the TX and the Receiver (RX), both with 1-bit element-wise phase control. A downlink (DL) transmission is emulated, where the TX (resp. the RX) plays the role of the Base Station (BS) (resp. UE). Both the layout of the reference indoor environment and the tested deployment configurations are represented in Fig. 2. Using a static beam, the BS illuminated the activated RIS, which was tested sequentially within two distinct location/orientation configurations. For each configuration, the RIS was controlled through a codebook to perform beam sweeping in azimuth from $-60°$ to $+60°$, by the step of $5°$. For both BS and RIS, a unique anticlockwise convention was used to define the AoDs, using a reference angle (i.e., $0°$) normal to the surface/array. The measurement procedure above was repeated over 5 main UE positions. For each of those positions, the RX monopole antenna was moved over a 3×3 small-scale grid (i.e., considering a virtual square array in the horizontal x-y plane) thanks to a high-precision positioner, and a frequency-domain complex channel response between the TX and the RX was recorded by the step of 10 MHz on each occupied small-scale position of the grid. Note that the three involved entities (i.e., BS, RIS and UE) were all set at the same height of 1.6m and hence, lying on the same 2D plane during all experiments. Further details about measurements calibration (e.g., effects of cables and RF components) can be found in [15].

Relying on the virtual array on the UE side, the classical Space-Alternating Generalized Expectation-maximization (SAGE) algorithm [18] was applied to different sub-bands (within bandwidths of 400 MHz, 2 GHz, and 4 GHz) centered around around 28 GHz, so as to extract the parameters of the most significant multipath components (MPCs), including the Angle of Arrival (AoA), power gain, and absolute delay.

B. Extraction of Location-dependent Radio Features

Like in [14], we first consider a situation where the RIS AoD would be directly determined through beam sweeping, based on the strongest power gains of resolved MPCs[1](i.e.,

[1]Estimated AoAs were used for spatially pre-filtering out the MPCs of interest in [14], although they could be used also for UE orientation estimation.

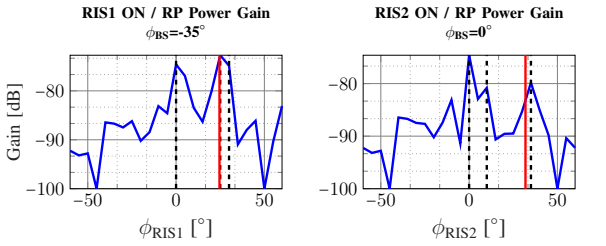

Fig. 3: RP power gain over RIS beam scanning w.r.t. the first tested UE location, as a function of steering angles ϕ_{RIS1} with $\phi_{BS} = -35°$ (left) or ϕ_{RIS2} with $\phi_{BS} = 0°$ (right), with ground-truth angles (solid red) and AoD angle candidates corresponding to the 3 strongest Rx power contributions at the UE (dashed black), based on real measurements from [14].

hopefully, the RIS Reflected Path (RP)) over all possible steering directions. Fig. 3 shows examples of such RIS AoD estimation, for a RP with respect to the first tested UE location (i.e., UE1) and the two distinct RIS locations. In this illustration, focusing on the three strongest power contributions, the selected angle candidates would be $\widetilde{\phi}_{RIS1} = 25°/0°/30°$ for a ground-truth angle of 24.6° (See Fig. 3 - left) and $\widetilde{\phi}_{RIS2} = 0°/35°/10°$ for a ground-truth angle of 31.9° (See Fig. 3 - right). As a counterpart to simplicity, this basic non-coherent method clearly suffers from the presence of strong grating lobes in the RIS beam patterns, which result in apparent local power maxima. The angular step of 5° applied for beam scanning is also quite large compared to the RIS -3dB beamwidth (i.e., below 3° for the considered prototype [16]). Accordingly, grating lobes can contribute even more than the apparent main lobe and the tested steering angle leading to the strongest power gain does not even always coincide with the best candidate, hence causing very large angular errors of several tens of degrees, even at short RIS-UE distances (See Fig. 1). These angular ambiguities motivate the need for efficient data association procedures to be able to exploit such measurements in positioning, while exploiting all the available information (i.e., over both MPCs and beam steering angles).

In addition to the previous AoDs, the calibrated absolute delays associated with the same MPCs extracted from SAGE (or equivalently, to within the speed of propagation, the estimated MPC distances traveled over-the-air) are also considered as an input to positioning (See Sec. III-A).

III. Positioning Approaches

A. Tested Scenarios

In all the tested configurations, we assume that both the positions and the orientations of BS and/or RIS are perfectly known. Moreover, unlinke in [14], we herein focus only on a single-BS RIS-aided DL positioning scenario, where the BS illuminates one single RIS at a time and the UE can rely on the received MPC signals after RIS reflection (i.e., incl. both natural BS-objects (walls, scatterers...)-UE MPCs and the BS-RIS-UE MPC controlled through RIS beam sweeping).

For RIS beam scanning, the current steering azimuth angle is indexed by $k = 1, 2, ..., K$. For each k, the UE resolves up to L_k MPCs indexed by l_k. For each l_k, we collect the corresponding tuple or parameters, composed of the MPC power gain (i.e., a shifted version of its received signal strength in a real system), time delay (as estimated by the SAGE algorithm), and AoD (i.e., the current steering angle), denoted by $\{P(l_k), \tau(l_k), \phi(l_k)\}$. The whole set of collected data is thus represented as follows: $\{\{P(l_k), \tau(l_k), \phi(l_k)\}_{l_k=1}^{L_k}\}_{k=1}^{K}$.

B. Compared Positioning Strategies

1) Method 1 (Shortest MPC): For each RIS beam steering angle, $k = 1, \ldots, K$, we first select the set of delay and AoD values corresponding to the MPC exhibiting the strongest power gain (over all the resolved components):

$$\{\bar{\tau}_k, \bar{\phi}_k\} = \{\tau(l_k^*), \phi(l_k^*)\}, \tag{1}$$

where $l_k^* = \text{argmax}_{l_k} P(l_k)$. Then, the assumed direct path between the BS and the UE is chosen as the MPC exhibiting the shortest delay (over all the tested steering angles):

$$\hat{k} = \text{argmin}_k \bar{\tau}_k. \tag{2}$$

This heuristic strategy is motivated by the empirical observation that the strongest MPC is still most often the direct one, even when the BS is illuminating the RIS [14]. Finally, the 2D position of the UE is simply estimated as

$$\mathbf{x}_{\text{UE}} = \mathbf{x}_{\text{BS}} - c\hat{\tau}\mathbf{g}(\hat{\phi}), \tag{3}$$

where $\{\hat{\tau}, \hat{\phi}\} = \{\bar{\tau}_{\hat{k}}, \bar{\phi}_{\hat{k}}\}$, c is the speed of propagation, and $\mathbf{g}(\cdot) = [\cos(\cdot), \sin(\cdot)]^\top$.

2) Method 2 (Strongest MPC): Similar to Method 1, for $k = 1, \ldots, K$, we first select the set of power gain, delay, AoD parameters associated with the MPC exhibiting the strongest power gain (over all the resolved components):

$$\{\bar{P}_k, \bar{\tau}_k, \bar{\phi}_k\} = \{P(l_k^*), \tau(l_k^*), \phi(l_k^*)\}, \tag{4}$$

where $l_k^* = \text{argmax}_{l_k} P(l_k)$. Then, we determine as the direct path, the MPC exhibiting the strongest channel gain (over all the tested steering angles):

$$\hat{k} = \text{argmax}_k \bar{P}_k. \tag{5}$$

The final positioning step is similar to (3) in Method 1.

3) Method 3 (Proposed approach): The posterior density used to estimate the UE position can be expressed as

$$f(\mathbf{x}_{\text{UE}}|Z) \propto f(\mathbf{x}_{\text{UE}}) \prod_j^J \prod_{i=\{\text{BS,RIS}\}} f(\mathbf{z}^j|\mathbf{x}_{\text{UE}}, \mathbf{x}_i) \tag{6}$$

$$= f(\mathbf{x}_{\text{UE}}) \sum_{a,b} \prod_j^J \prod_{i=\{\text{BS,RIS}\}} f(\mathbf{z}^j|\mathbf{x}_{\text{UE}}, \mathbf{x}_i, a^i, b^j) \times \psi(a^i, b^j), \tag{7}$$

where $Z = \{\mathbf{z}^1, ..., \mathbf{z}^j, ..., \mathbf{z}^J\}$ is the set of all observations[2] (i.e., over both MPCs and beam steering angles), with $\mathbf{z}^j$ the tuple of power gain, time delay, and beam steering angle associated with the j-th observation, $f(\mathbf{x}_{\text{UE}})$ is the UE prior density, $f(\mathbf{z}^j|\mathbf{x}_{\text{UE}}, \mathbf{x}_i, a^i, b^j)$ is the likelihood function for

[2]Note that the total number $\sum_k L_k$ of extracted MPCs is not equal to the number of observations J due to missed detections or false alarms, while the vector $\mathbf{b}$, which indicates an observation-oriented association, is of length J.

observation j with respect to source i with the association variables $\mathbf{a} = [a^{\mathrm{BS}}, a^{\mathrm{RIS}}]^\top$ where $a^i \in \{1, ..., J\}$ for $i = \{\mathrm{BS}, \mathrm{RIS}\}$, $\mathbf{b} = [b^1, \ldots, b^J]^\top$, and $\psi(a^i, b^j) = 1$ under a valid association between a^i and b^j, or 0 otherwise (given one-to-one mapping, i.e., that the knowledge of a^i directly provides b^j). The BS and the RIS, whose positions are respectively depicted by $\mathbf{x}_{\mathrm{BS}}$ and $\mathbf{x}_{\mathrm{RIS}}$, serve here as known static sources (i.e., as anchors). To implement the above posterior density needed for UE positioning while jointly handling the data association problem, we thus adapt a set-type Simultaneous Localization And Mapping (SLAM) algorithm from [19] to a single snapshot, as follows:

a) Prediction Step: The UE prior follows a Gaussian distribution $f(\mathbf{x}_{\mathrm{UE}}) = \mathcal{N}(\bar{\boldsymbol{\mu}}_{\mathrm{UE}}, \bar{\boldsymbol{\Sigma}}_{\mathrm{UE}})$, where:

- $\bar{\boldsymbol{\mu}}_{\mathrm{UE}}$ is the mean, computed as (3) of Method 1;
- $\bar{\boldsymbol{\Sigma}}_{\mathrm{UE}}$ is the covariance, a design parameter that we empirically set a priori.

b) Update Step: One can easily draw the factor graph of (7) by modifying that of [19, Fig. 5]. Then, the messages are computed by running the standard set-type belief propagation algorithm onto this modified factor graph.

For algorithmic simplicity, we determine the most likely single data association by making hard decisions via belief propagation [19, Sec. IV.C]. Finally, the UE posterior density computation follows the same approach as that used for the mobile state update in the SLAM algorithm [19], [20], except for the BS and RIS obviously.

This approach is expected to mitigate the geometric ambiguities that would be induced by irregular RIS beam patterns in case of direct power-based AoD interpretation (See II-B), by leveraging all the available MPC information over all the tested beam steering angles. Due to space limitations, we deliberately omit details about the underlying geometric models and intermediary implementation steps, which can be found in [19], [20].

IV. Experimental Results

In Fig. 4 and Fig. 5, we show the 2D positioning errors (in log scale) achieved with the three methods of Sec. III-A for different bandwidths, respectively for a RIS located in RRIS1 or RRIS2. For both tested RIS locations, the application of a data association step between the sources (i.e., BS and the RIS) and the MPCs (i.e., measurements) in the proposed method thus enables to globally maintain the best possible single-BS RIS-aided positioning performance, even in UE location indexes 4 and 5 where other methods based on heuristics would be significantly penalized by large RIS-UE ranges and/or Non-Line-of-Sight (NLoS) conditions between the BS and the UE. One second remark is that the proposed method also gradually benefits from the better time resolution allowed in SAGE estimation by the occupation of larger and larger bandwidths, hence improving further positioning accuracy accordingly, while other methods still suffer from a much more erratic behavior caused by geometric ambiguities and the selection of bad RIS AoD candidates, despite the enhanced time resolution.

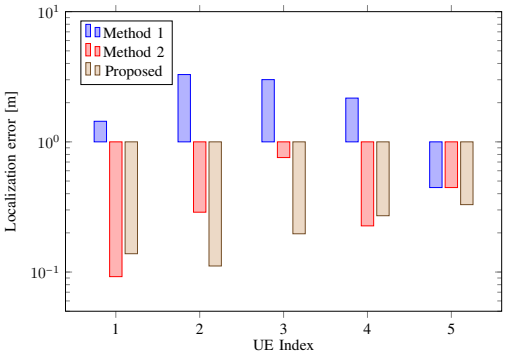

(a) 400 MHz BW

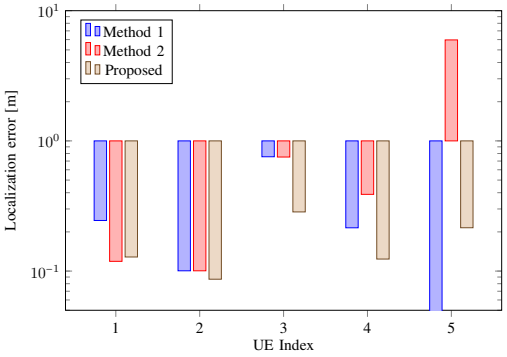

(b) 2000 MHz BW

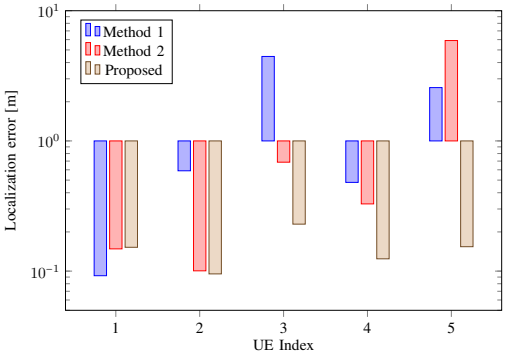

(c) 4000 MHz BW

Fig. 4: 2D localization error of single-BS RIS-aided positioning for a RIS in location RRIS1, as a function of the UE location index and bandwidth.

V. Conclusion and Future Work

In this paper, we account for experimental validations of a single-BS positioning system assisted by RIS beam sweeping, which is robust against the harmful effects caused by the irregular beam patterns and/or grating lobes of low-complexity reflective RIS. For this purpose, we have introduced an algorithmic approach inspired from SLAM processing that combines data association and positioning in a single Bayesian framework, where the prior density is determined by the MPC exhibiting the shortest time delay, while the posterior density is computed with channel parameters corresponding to all other resolved multipath components. Results based on real frequency domain mmWave channel sounding measurements in different bands centered around 28 GHz show that this approach preserves the best achievable 2D accuracy in single-BS RIS-aided DL positioning, by leveraging all the available

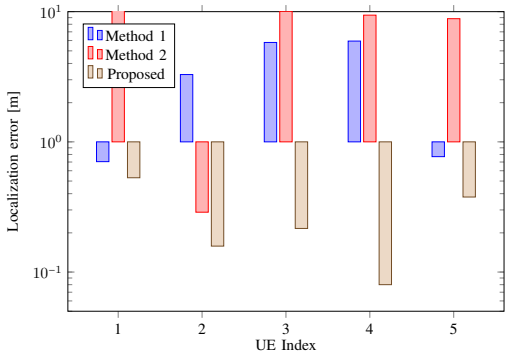

(a) 400 MHz BW

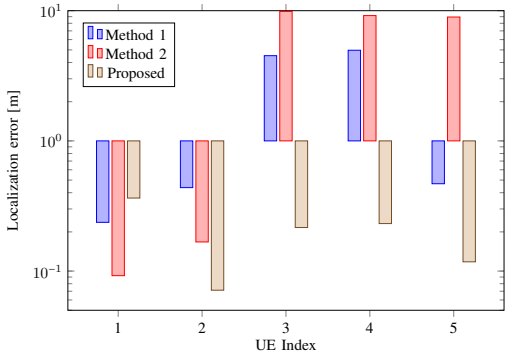

(b) 2000 MHz BW

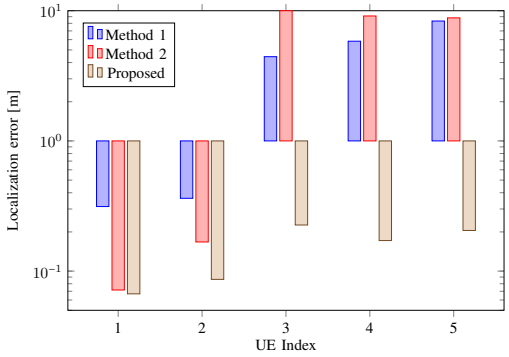

(c) 4000 MHz BW

Fig. 5: 2D localization error of single-BS RIS-aided positioning for a RIS in location RRIS2, as a function of the UE location index and bandwidth.

information at the UE (i.e., over both MPCs and RIS steering angles), even in presence of ambiguous received power readings that would cause large AoD errors when interpreted independently within conventional approaches [14].

Leveraging both the same DL RIS beam sweeping protocol, as well as the same experimental measurement data, future works will focus on opportunistic sensing applications, aiming at detecting passive objects in the UE vicinity.

ACKNOWLEDGMENT

The work of CEA researchers was supported by the European Commission through the Horizon Europe SNS-JU project 6G-BRICKS (grant agreement no. 101096954) and the French National Research Agency (ANR-22-PEFT-0005), as part of France 2030 through the NF-YACARI project.

REFERENCES

[1] G. C. Alexandropoulos, et al., "RIS-enabled Smart Wireless Environments: Deployment Scenarios, Network Architecture, Bandwidth and Area of Influence," *EURASIP Journal on Wireless Communications and Networking*, Oct. 2023.

[2] E. Calvanese-Strinati, et al., "Reconfigurable, Intelligent, and Sustainable Wireless Environments for 6G Smart Connectivity," *IEEE Communications Magazine*, vol. 59, pp. 99–105, Oct. 2021.

[3] K. Keykhosravi, et al., "Leveraging RIS-Enabled Smart Signal Propagation for Solving Infeasible Localization Problems: Scenarios, Key Research Directions, and Open Challenges," *IEEE Vehicular Technology Magazine*, vol. 18, pp. 20–28, Feb. 2023.

[4] H. Wymeersch, et al., "Radio Localization and Mapping With Reconfigurable Intelligent Surfaces: Challenges, Opportunities, and Research Directions," *IEEE Vehicular Technology Magazine*, vol. 15, pp. 52–61, Oct. 2020.

[5] H. Wymeersch and B. Denis, "Beyond 5G Wireless Localization with Reconfigurable Intelligent Surfaces," in *Proc. IEEE International Conference on Communications 2020*, June 2020.

[6] A. Elzanaty, et al., "Reconfigurable Intelligent Surfaces for Localization: Position and Orientation Error Bounds," *IEEE Transactions on Signal Processing*, vol. 69, pp. 5386–5402, Aug. 2021.

[7] J. He, et al., "Large Intelligent Surface for Positioning in Millimeter Wave MIMO Systems," in *Proc. IEEE Vehicular Technology Conference 2020 - Spring*, May 2020.

[8] H. Zhang, et al., "Towards Ubiquitous Positioning by Leveraging Reconfigurable Intelligent Surface," *IEEE Communications Letters*, vol. 25, pp. 284–288, Jan. 2021.

[9] K. Keykhosravi, et al., "SISO RIS-enabled Joint 3D Downlink Localization and Synchronization," in *Proc. IEEE International Conference on Communications 2021*, June 2021.

[10] M. Rahal, et al., "RIS-enabled Localization Continuity Under Near-Field Conditions," in *Proc. IEEE International Workshop on Signal Processing Advances in Wireless Communications 2021*, Sept. 2021.

[11] M. Rahal, et al., "Constrained RIS Phase Profile Optimization and Time Sharing for Near-field Localization," in *Proc. IEEE Vehicular Technology Conference 2022 - Spring*, June 2022.

[12] Y. Liu, et al., "Reconfigurable Intelligent Surface Aided Wireless Localization," in *Proc. IEEE International Conference on Communications 2021*, June 2021.

[13] M. Rahal, et al., "Performance of RIS-Aided Nearfield Localization under Beams Approximation from Real Hardware Characterization," *EURASIP Journal on Wireless Communications and Networking*, Aug. 2023.

[14] M. Rahal, et al., "RIS-aided Positioning Experiments based on mmWave Indoor Channel Measurements," in *Proc. International Conference on Indoor Positioning and Indoor Navigation 2023*, pp. 1–6, Sept. 2023.

[15] T. Mazloum, et al., "Impact of Multiple RIS on Channel Characteristics: an Experimental Validation in Ka Band," in *Proc. Joint European Conference on Networks and Communications & 6G Summit 2023*, June 2023.

[16] J.-B. Gros, et al, "A Reconfigurable Intelligent Surface at mmWave Based on a Binary Phase Tunable Metasurface," *IEEE Open Journal of the Communications Society*, vol. 2, pp. 1055–1064, May 2021.

[17] L. Di Palma, et al., "1-Bit Reconfigurable Unit Cell for Ka-Band Transmitarrays," *IEEE Antennas and Wireless Propagation Letters*, vol. 15, pp. 560–563, July 2015.

[18] K. Haneda and J.-I. Takada, "An Application of SAGE Algorithm for UWB Propagation Channel Estimation," in *Proc. IEEE Conference on Ultra Wideband Systems and Technologies 2003*, Nov. 2003.

[19] H. Kim, et al., "Set-Type Belief Propagation with Applications to Poisson Multi-Bernoulli SLAM," *IEEE Transactions on Signal Processing*, vol. 72, pp. 1989–2005, April 2024.

[20] H. Kim, et al., "RIS-Enabled and Access-Point-Free Simultaneous Radio Localization and Mapping," *IEEE Transactions on Wireless Communications*, vol. 23, pp. 3344–3360, April 2024.